



# Measurement and calibration of rotor/touchdown bearing contact in active magnetic bearing systems



F.Y. Saket, M.N. Sahinkaya, P.S. Keogh\*

Department of Mechanical Engineering, University of Bath, Bath BA2 7AY, UK

## ARTICLE INFO

### Article history:

Received 23 November 2017  
 Received in revised form 14 June 2018  
 Accepted 5 December 2018  
 Available online 20 December 2018

### Keywords:

Rotor touchdown contact  
 Strain measurement  
 Contact rotor dynamics  
 Active magnetic bearing  
 Touchdown bearing

## ABSTRACT

Active magnetic bearing systems provide contact-free rotor levitation, which allows near frictionless rotation and high rotational speeds when they operate normally. Under certain operational conditions, a transient fault, overload condition, or disturbance may occur. Touchdown bearings or bushings are therefore implemented in such systems to prevent contact between rotor and stator laminations. If the rotor makes contact with a touchdown bearing, the rotor dynamics may become transient or persistent in contact. Appropriate control strategies through the magnetic bearings to restore contact-free rotor operation may extend the life of touchdown bearings, and minimise operational downtime. To achieve this, an understanding of the contact dynamics is required, together with the relationship between contact and magnetic bearing forces. In this paper, rotor/touchdown bearing contact conditions are investigated experimentally using an active magnetic bearing system with a flexible rotor. Design methodology is presented for a measurement system capable of providing rotor/touchdown bearing contact related data, based on strain measurement. Strain induced contact signals are calibrated against applied magnetic bearing forces. The frequency dependent behaviour of the active magnetic bearing system is considered using evaluated force and phase measurements. The measurement data represent system identification for the potential of active magnetic bearing force-based contact control.

© 2018 Elsevier Ltd. All rights reserved.

## 1. Introduction

The ability of Active Magnetic Bearings (AMBs) to provide contactless rotor levitation with vibration control has a number of benefits, including high-speed rotor operation, the elimination of the need for lubrication, long life and reliability, and energy efficiency due to the low friction losses. However, passive bearings are also used in AMB systems as Touchdown Bearings (TDBs) to prevent potentially damaging rotor/magnetic bearing stator contact from occurring. TDBs support the rotor while the AMB system is not operating, but also limit excursions of the rotor during operation, such as in cases of power loss, component failure, rotor mass loss, or other significant external disturbances. Such cases may cause rotor/TDB contact. Since TDBs are functional components of AMB systems, it is crucial to understand their influence on rotor dynamic behaviour in contact cases, in order to minimise potential damage. This is particularly important as TDB life and condition impacts directly on the reliability of AMB systems.

\* Corresponding author.

E-mail address: [p.s.keogh@bath.ac.uk](mailto:p.s.keogh@bath.ac.uk) (P.S. Keogh).

Rotor/TDB contact interaction has been investigated in several studies. Rotor drop tests have been considered [1–5]. The effects of contacts occurring inside the TDB have also been investigated, where TDB degradation was considered [6]. While rigid rotor setups have been studied widely, flexible rotor systems have also been considered [7–9]. Different numerical models and experimental setups used in studying contact cases have been reviewed, where the complexity of contact dynamics was highlighted and discussed [10]. Contact modes reported and studied as a result of rotor/TDB interaction include rubs [11–14], bounces [15] and chaotic responses [16,17]. These modes vary in duration and can involve large contact stresses and strains experienced by a TDB. An interesting approach involving a rainflow counting algorithm to predict rolling element TDB life has been proposed in [18].

Methods have been considered in the literature to attenuate rotor vibration upon contact with a TDB, in order to minimise or eliminate contact. Unconventional TDB design has been considered to moderate impact induced motion and frictional forces, particularly to prevent the backward whirl motion [19]. The use of ribbon dampers to support TDBs is assessed by nonlinear modelling and experiment in [20,21]. Magnetic bearing contact control has been investigated, where the importance of incorporating rotor/TDB contact dynamics into the controller design was demonstrated [22,23]. Control employing TDB motion has been considered in other studies [24–28]. In contrast to magnetic bearing control, employing active TDBs involves increased cost and added complexity, although it may be useful in certain cases where extra actuation is needed.

Rotor/TDB contact attenuation, recovery and potential prevention with operational AMBs has been considered in the literature, where rotor displacement data were employed [26,29,30]. However, experimental force data, if made available, could provide further knowledge of the interaction dynamics and enable optimisation of the control action to reduce or eliminate the damaging effects of contact.

Some studies have considered the measurement and analysis of forces relating to contact conditions [12,31–33]. Different ways have been used to assess experimentally force levels experienced by a bearing upon rotor contact, by incorporating sensors within the TDB or its housing. This includes the use of piezoelectric force transducers [33,34], acceleration data [35], and the measurement of strain [36]. Devising rotor/TDB contact control strategies based on force data in operational AMB systems is an area requiring further research. This is particularly significant if AMBs can remain fully functional in contact cases.

To devise force-based contact control in rotor/AMB/TDB systems, a method of obtaining data related to rotor/TDB contact induced by AMB control forces would be useful. The aim of this paper is to provide such experimental data that could be directly applicable in future rotor/TDB contact control strategies if appropriately phased AMB synchronous forces are employed. The relationships between rotor/TDB interaction forces and AMB control forces are established over different rotor forcing frequencies, including those that encompass critical speed frequencies.

## 2. Experimental rotor/AMB system

A rotor/AMB test rig with a flexible rotor was employed. The system has two radial AMBs, a rotor with four discs, position transducers providing rotor displacement signals, and an AC motor at one end. A photograph of the experimental facility is shown in Fig. 1. The flexible rotor is 2 m long with a shaft radius of 25 mm. There is a radial clearance of 1.2 mm between the stator and rotor in each of the magnetic bearings. A number of conventional TDBs are used in the system. At each magnetic bearing location, there is a rolling element TDB with a radial clearance of 0.75 mm. In addition, a bronze bush is placed at the driven end of the rotor, with a radial clearance of 0.90 mm. A strain measurement system was designed and installed at the non-driven end of the rotor to provide force data related to rotor/TDB contact, which is described in the next section. Closed loop feedback control was used to operate the AMBs, each of which had a radial force saturation limit of 2000 N. The controllers for both AMBs use eddy current position transducer signals. Fig. 2 shows the layout of the components of the test rig.

The total rotor mass was 100 kg and under specific Proportional-Integral-Derivative (PID) levitated control without any contact, conical and translatory rotor whirl modes were evident at 12 Hz and 17 Hz, respectively, and the first levitated rotor flexure mode had a natural frequency of 27 Hz. The bandwidth of the AMB amplifier system was approximately 120 Hz. The

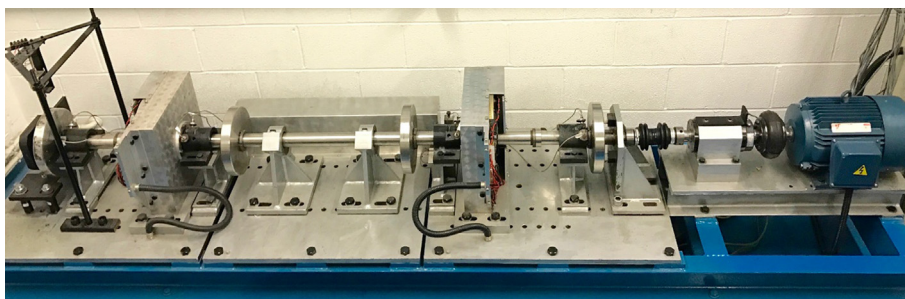


Fig. 1. The rotor/active magnetic bearing experimental facility.

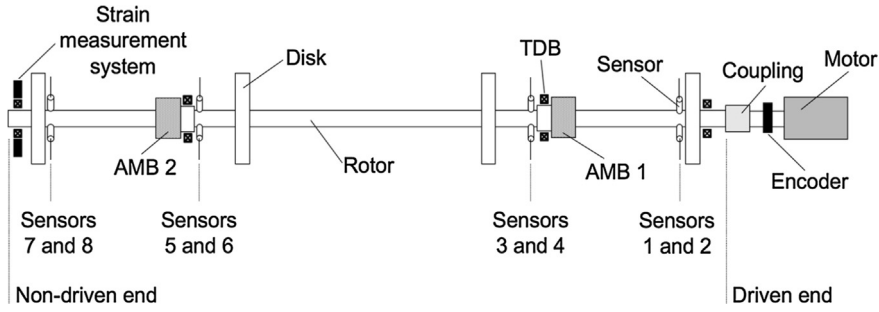


Fig. 2. Schematic layout of the experimental facility.

rotor/AMB/base frame system was mounted on resilient isolators to ground and a horizontal lateral mode at 7 Hz was also evident. Under rub-contact conditions these frequencies will be modified depending on the level of contact force.

### 3. Strain measurement system

To assess experimentally the behaviour of the rotor/bearing system under dynamic contact conditions, a method of relating contact-induced strains to applied magnetic bearing forces was devised. Fig. 3 shows the generic approach. Here,  $\hat{\mathbf{f}}_{MB}(t)$  is a vector of harmonic force components inputted through the AMB system at frequency  $\omega$ , and  $\mathbf{f}_c(t)$  is a vector of induced contact force components. The vector  $\hat{\mathbf{v}}(t)$  contains measurable voltage components that are output from the strain measurement system. Estimated pseudo-dynamic AMB force components based on a static calibration procedure are contained in the vector  $\mathbf{f}_{MB}^{ep}(t)$ . The input force and frequency dependent scalar factor  $\alpha(\hat{\mathbf{f}}_{MB}, \omega)$  relates norms of the estimated pseudo-dynamic AMB force and applied AMB force components. It allows a vector of estimated dynamic AMB force components in  $\mathbf{f}_{MB}^e(t)$  to be compared against the inputted AMB force components in  $\hat{\mathbf{f}}_{MB}$ . The procedural steps include:

- (a) The strain measurement system is calibrated under static conditions by applying constant AMB forces.
- (b) Harmonic AMB forces are then applied and the pseudo-dynamic force components are estimated using the static calibration coefficients.
- (c) The ratio of the estimated pseudo-dynamic AMB force norm to the applied dynamic AMB force norm is used to derive the dynamic scalar factor,  $\alpha(\hat{\mathbf{f}}_{MB}, \omega)$ .

To implement the steps of Fig. 3, a system based on strain gauge measurements was designed, commissioned and mounted onto the rotor/AMB test facility. The system was designed to respond to contact between the rotor and a TDB at the non-driven end of the rotor and hence provide experimental data over a range of contact conditions.

#### 3.1. Design and transducer considerations

Many types of transducer exist that can provide force related data. To assess rotor/TDB contact the choice of a transducer type and measurement system design was based on a number of considerations, including:

- (a) The range of AMB forces that could be applied to induce contact.
- (b) Measurement of contact force components. This involves the ability to identify forces acting on the system, to infer their directions, and corresponding phases.

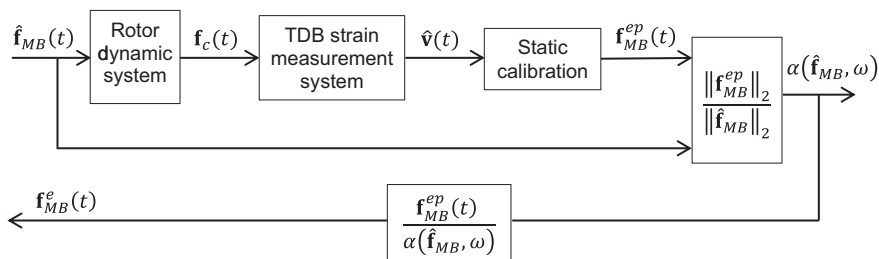


Fig. 3. Procedure to assess contact induced dynamics.

- (c) Capability of dynamic measurements. The system was required to be capable of measuring dynamic force related data, given the dynamic loading conditions of contact events.
- (d) Appropriate size and installation. The system incorporating the TDB and the measurement transducers should have an appropriate size, and the design must allow installation within the space available to mount the device at the non-driven end of the experimental rig.

A design incorporating strain gauges mounted on elastic elements was selected, which has the advantage of providing a continuously stable response and responding to contact forces with relatively high linearity from elastic strains. This is particularly useful for the measurement of persistent contact forces. Strain gauges are capable of measuring in static and dynamic loading conditions, and can provide an adequate frequency range for the application considered. They provide the flexibility of integration into a variety of systems and designs.

### 3.2. System description

A TDB support structure with elastic elements was designed to withstand the expected loading conditions. The system consists of a steel housing, containing a bronze bush acting as a TDB, supported by three cylindrical aluminium support beams acting as the elastic elements of the system. Each beam is 40 mm long, with a radius of 5 mm. The beams were equipped with strain gauges, and were mounted on a steel structure. The system was 30 mm wide and thus covered 30 mm of the 2 m rotor length at the non-driven end of the rotor. A steel sleeve and collar were mounted onto the rotor at the measurement system location, providing a radial rotor/TDB clearance of 0.35 mm under controlled rotor levitation by the AMBs. Fig. 4 shows the strain measurement system.

The natural frequencies of the steel housing and TDB on the beam supports were approximately 1320 Hz in the  $y$  direction and 930 Hz in the  $x$  direction, which are significantly higher than the operating frequency range of the rotor system. The difference was due primarily to the extra stiffness of two support beams in tension and compression in the  $y$  direction. The strain gauges and their amplifiers alone had a combined bandwidth that exceeded both natural frequencies; hence, the limitation of the overall strain measurement system was due to the mechanical resonances. The use of two support beams in the vertical direction also enhanced the static stability of the rotor weight supported at the non-driven end by the bronze TDB when the AMBs were switched off. The two vertical support beams also aid identification of vertical and rotational motions of the steel housing in the plane of the TDB.

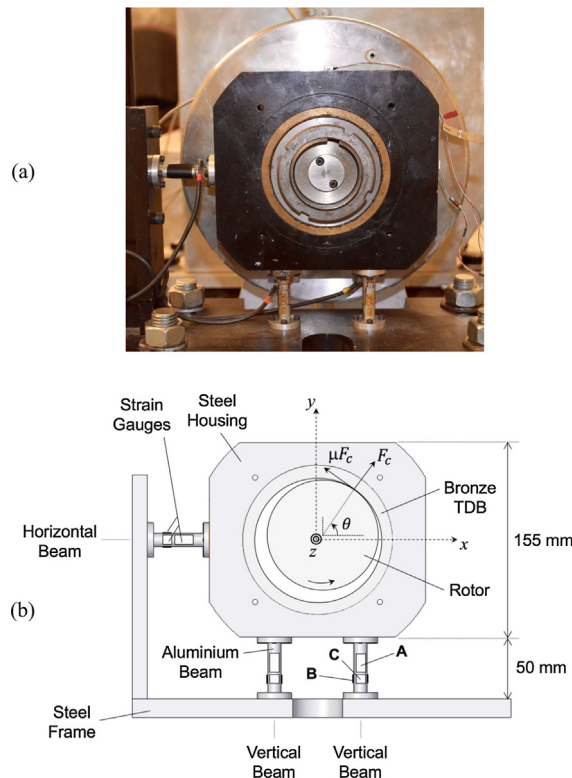


**Fig. 4.** TDB strain measurement system layout: (a) Photograph showing the rotor with the sleeve and collar. (b) Schematic including rotor contact forces acting on the TDB.

The procedure for assessing the level of contact was to record the signals from the strain measurement system when rotor/TDB interactions occur. These led to force transmission hence to elastic deformation of the three support beams. Since rotor/TDB contact can occur at any point or angle on the TDB inner surface, this dictated the use of pairs of strain gauges on the beams in more than one arrangement. The strain gauges were arranged to deflect under tension, compression, and bending strains in the beams.

In total, 9 pairs of strain gauges were used on the support beams, with 3 pairs on each. Each pair was attached to a beam on opposing sides at the same location along the length of the beam to detect the required strains. The system design and strain gauge layout enables the system to be sensitive to three orthogonal force components, which are the  $x$  and  $y$  radial force components, and the  $z$  axial force component from the rotor. The coupling that connected the rotor to the motor was laterally flexible and axially stiff, hence the rotor axial motion ( $<0.01$  mm) was an order of magnitude smaller than rotor radial motion (up to 0.75 mm at AMB 2 and 0.35 mm at the strain measurement end TDB). Thus axial contact forces were correspondingly smaller than the radial contact forces that influence the rotor radial motion and so were not considered in the assessment of forces in Fig. 3. A combination of full and half Wheatstone bridge circuits were used in the system instrumentation, giving 9 voltage output signals. Fig. 4(b) indicates the strain gauges attached to the beams. Strain gauge (A) is one of two identical gauges attached to each beam on opposite sides. This strain gauge has two gauges built-in. The first measures beam tension and compression strains, and the second acts as a Poisson gauge. Each pair of opposing strain gauges (A) thus has four active gauges, which are connected to a full Wheatstone bridge, providing strain measurements relating to tension and compression in each beam. The pair of opposing strain gauges (B) on each beam is connected to a half Wheatstone bridge circuit, providing beam bending related measurements, while rejecting any beam tension/compression strains. The same applies for strain gauge pairs (C) on each beam, which measure bending strains associated with moments in the axial plane.

The bandwidth of the strain gauge system was 108 Hz, which provided an adequate dynamic response for the results presented. The beam length and radius dimensions were chosen so that they produce enough measurable strain for relatively small applied forces, while also withstanding forces higher than the operating range, and providing enough space to mount the strain gauges.

## 4. Strain measurement calibration

### 4.1. Methodology

To establish a relationship between AMB forces and estimated forces related to rotor/TDB contact, force components related to rotor/TDB contact were calibrated against input forces applied by an AMB (Fig. 3). Such a relationship would provide important force data that could be used in future rotor/TDB interaction control.

The calibration procedure took into account the 9 strain gauge outputs provided by the system. Forces  $\mathbf{f}_{MB}$  were applied through AMB 2 after the rotor was levitated, to induce rotor/TDB contact forces  $\mathbf{f}_c$  at the measurement system (Fig. 5). The measurements of the resulting voltages of the strain gauges were then related to the AMB 2 forces in the two radial components, and then to the phase angles, to achieve the calibration of radial forces measurement in the system.

The applied AMB 2 force  $\mathbf{f}_{MB}$  is expressed as a  $2 \times 1$  rotating force vector consisting of  $x$  and  $y$  components as

$$\mathbf{f}_{MB}(t) = \begin{bmatrix} f_{MBx}(t) \\ f_{MBy}(t) \end{bmatrix} = \begin{bmatrix} F_{MB} \cos(\omega t + \phi_{MB}) \\ F_{MB} \sin(\omega t + \phi_{MB}) \end{bmatrix} \quad (1)$$

where  $\omega$  is the forcing frequency applied by AMB 2. Also,  $F_{MB}$  is the force amplitude and  $\phi_{MB}$  is the phase angle. The forcing of Eq. (1) is circular, analogous to unbalance excitation. The corresponding contact force vector  $\mathbf{f}_c$  in  $x$  and  $y$  components at the measurement location is written as

$$\mathbf{f}_c(t) = \begin{bmatrix} f_{cx}(t) \\ f_{cy}(t) \end{bmatrix} = \begin{bmatrix} F_c \cos(\omega t + \phi) \\ F_c \sin(\omega t + \phi) \end{bmatrix} \quad (2)$$

Assuming that the strain measurement system is linear, the contact force can be related to the strain gauge voltages by

$$\mathbf{f}_c(t) = \mathbf{C}_c(\omega)\mathbf{v}(t) \quad (3)$$

where  $\mathbf{C}_c(\omega)$  is a calibration matrix and  $\mathbf{v}(t)$  is a  $9 \times 1$  voltage vector of the strain gauge voltage output signals. Under steady conditions ( $\omega = 0$ ), the contact force can be related to the applied AMB 2 force by considering moments about the AMB 1 location (see Fig. 5), where the rotor is considered to be centralised by PID control action:

$$\mathbf{f}_c(t) = \left( \frac{l_1 - l_2}{l_1} \right) \mathbf{f}_{MB}(t) \quad (4)$$

Substituting Eq. (4) into Eq. (3), with  $\omega = 0$ , yields the AMB 2 force as

$$\mathbf{f}_{MB}(t) = \mathbf{C}_{MB}(0)\mathbf{v}(t) \quad (5)$$

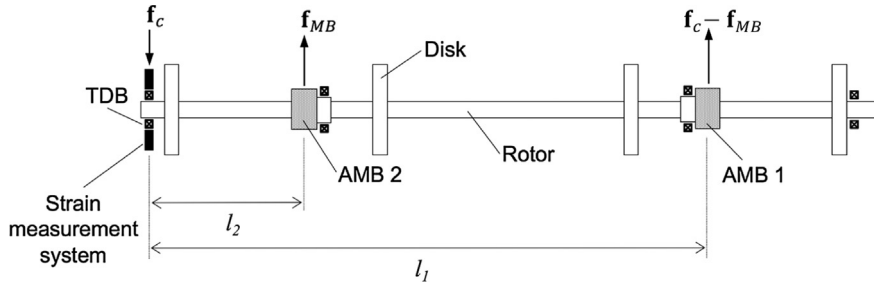


Fig. 5. Schematic layout of the test rig showing AMB and contact forces applying to the rotor.

where  $\mathbf{C}_{MB}(\omega)$  is a frequency dependent calibration matrix relating applied AMB 2 forces to strain gauge voltages upon rotor/TDB contact, defined as

$$\mathbf{C}_{MB}(0) = \left( \frac{l_1}{l_1 - l_2} \right) \mathbf{C}_c(0) \quad (6)$$

Eq. (5) represents the static ( $\omega = 0$ ) calibration due to applied AMB 2 forces and the strain measurement system output voltages.

#### 4.2. Static tests

Employing static AMB 2 forces, experimental tests were performed to calibrate the strain measurement system. Both the applied whirl frequency of the AMB and the rotational (motor) frequency were set to zero. Different force amplitudes and phase angles were applied through AMB 2, which is closest to the strain measurement system. The integral control action was switched off at AMB 2 during tests, while the integral control action at AMB 1 kept the rotor centralised at its normal operating point. Rotor/TDB contact due to static AMB 2 applied forces only occurred at the strain measurement system location. Static tests were undertaken with a series of input AMB 2 radial forces ranging from 100 N to 2000 N, over 8 input phase angles covering 360 deg. The AMB force amplitudes are represented in

$$\hat{\mathbf{F}}_{MBn}(0) = [\hat{\mathbf{f}}_{MBn,1}(0), \dots, \hat{\mathbf{f}}_{MBn,8}(0)] \quad (7)$$

where  $n = 1, \dots, 12$ , correspond with the 12 input force amplitudes. Here,  $\hat{\mathbf{f}}_{MBn,j}(0)$  is a  $2 \times 1$  input force amplitude vector, with  $\omega = 0$ , of the x and y components of a given input amplitude,  $\hat{\mathbf{F}}_{MBn}$ :

$$\hat{\mathbf{f}}_{MBn,j}(0) = \begin{bmatrix} \hat{f}_{MBnx,j} \\ \hat{f}_{MBny,j} \end{bmatrix} = \begin{bmatrix} \hat{F}_{MBn} \cos \hat{\phi}_{MBj} \\ \hat{F}_{MBn} \sin \hat{\phi}_{MBj} \end{bmatrix} \quad (8)$$

applied at 8 different input phase angles,  $\hat{\phi}_{MB1}, \dots, \hat{\phi}_{MB8}$ . The corresponding voltage signals obtained with  $\omega = 0$  for each applied input AMB force amplitude are represented by

$$\hat{\mathbf{V}}_n(0) = [\hat{\mathbf{v}}_{n,1}(0), \dots, \hat{\mathbf{v}}_{n,8}(0)] \quad (9)$$

where  $\hat{\mathbf{V}}_n(0)$  is a  $9 \times 8$  matrix. Combining the 12 matrices resulting from Eq. (7), which correspond to the 12 force amplitudes, yields the overall applied forcing matrix, which consists of the 12 input force amplitudes, each applied at the 8 phase angles, as

$$\hat{\mathbf{F}}_{MB}(0) = [\hat{\mathbf{F}}_{MB1}(0), \dots, \hat{\mathbf{F}}_{MB12}(0)] \quad (10)$$

where  $\hat{\mathbf{F}}_{MB}$  is a  $2 \times 96$  matrix consisting of the x and y components of the 96 applied AMB 2 forces. The corresponding measured voltage signals may be assembled into

$$\hat{\mathbf{V}}(0) = [\hat{\mathbf{V}}_1(0), \dots, \hat{\mathbf{V}}_{12}(0)] \quad (11)$$

where  $\hat{\mathbf{V}}$  is a  $9 \times 96$  matrix.

In principle, the relationship between the AMB 2 input forces and the measured voltages can be expressed as

$$\hat{\mathbf{F}}_{MB}(0) = \mathbf{C}_{MB}(0) \hat{\mathbf{V}}(0) \quad (12)$$

Thus, a calibration matrix, representing the AMB force-strain voltage relationship, can be estimated as

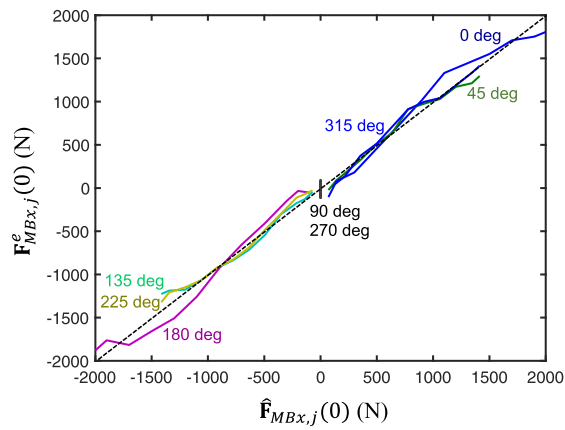


**Fig. 6.** x-Axis static input and estimated AMB 2 forces at phase angles: 0, 45, 90, 135, 180, 225, 270, and 315 deg. The dashed line (—) shows the idealized relation.

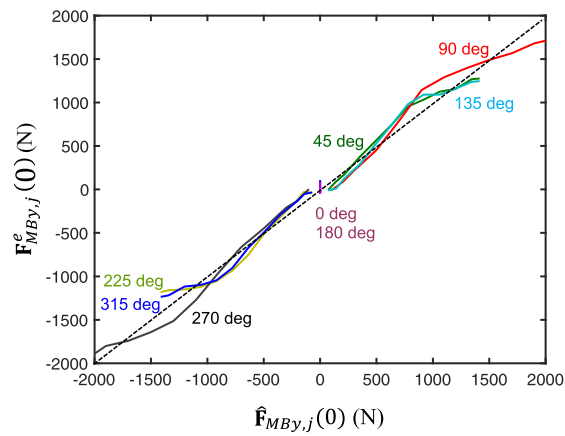


**Fig. 7.** y-Axis static input and estimated AMB 2 forces at phase angles: 0, 45, 90, 135, 180, 225, 270, and 315 deg. The dashed line (—) shows the idealized relation.

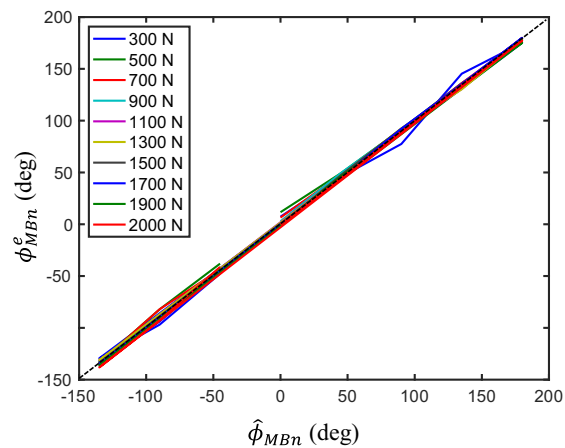


**Fig. 8.** Input and estimated phase angle variation with static AMB 2 forces over an input force range of 300–2000 N. The dashed line (—) shows the idealized relation.

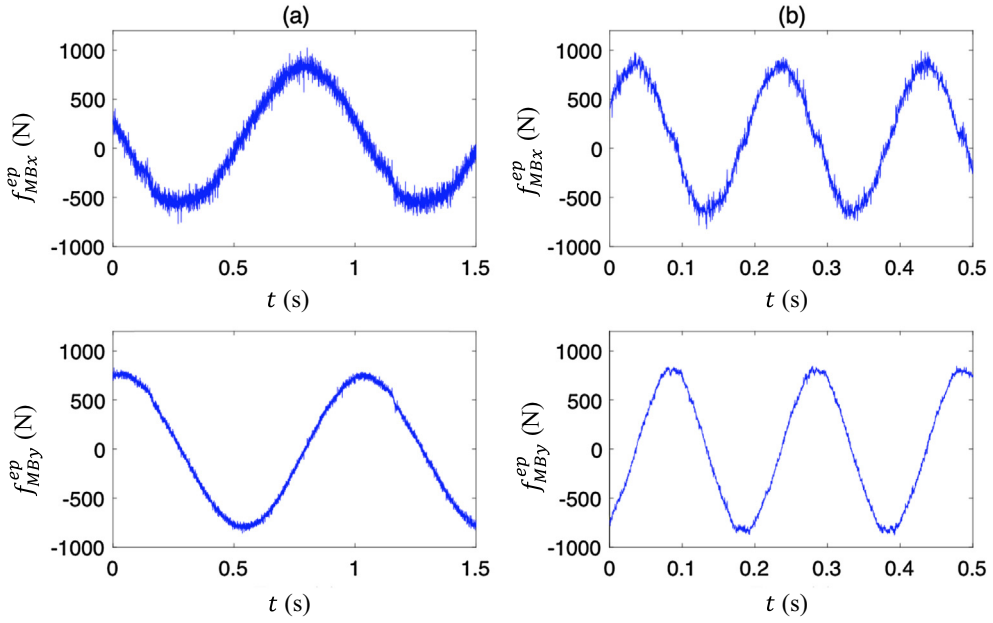


**Fig. 9.** Estimated pseudo-dynamic AMB 2 force x and y components for an AMB 2 applied force input of 700 N at (a) 1 Hz (b) 5 Hz.

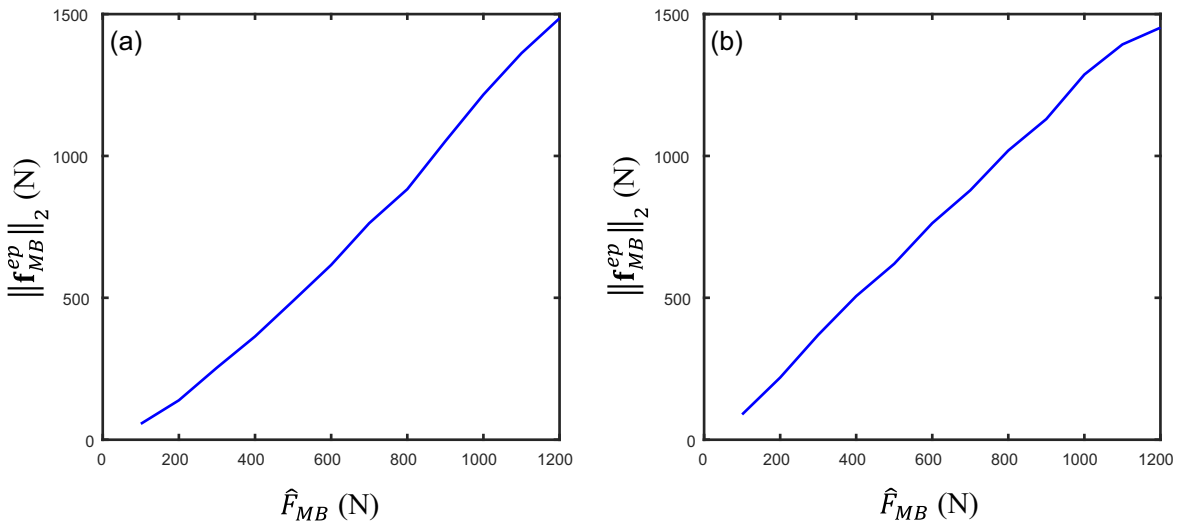


**Fig. 10.** Relationship between estimated pseudo-dynamic AMB 2 forces and input AMB 2 forces covering an input force range of 100–1200 N at (a) 1 Hz and (b) 10 Hz.

$$\mathbf{C}_{MB}^e(0) = \hat{\mathbf{F}}_{MB}(0) \hat{\mathbf{V}}^T(0) \left( \hat{\mathbf{V}}(0) \hat{\mathbf{V}}^T(0) \right)^{-1} \quad (13)$$

where  $\mathbf{C}_{MB}^e$  has dimensions  $2 \times 9$ . This calibration matrix is estimated in the presence of measurement error and nonlinearity. The AMB 2 forces corresponding to the 12 different input force amplitudes, which were applied in the static tests performed, may be estimated in a least squares sense as

$$\mathbf{F}_{MBn}^e(0) = \mathbf{C}_{MB}^e(0) \hat{\mathbf{V}}_n(0) \quad (14)$$

Figs. 6 and 7 show the relationships between the input forces and the estimated forces, in the x and y components, respectively, for the whole range of forces and angles used in the static tests. Fig. 8 shows the relationship between the input and estimated phase angles. Each estimated phase angle,  $\phi_{MBn}^e$ , was obtained using the corresponding x and y components of the estimated force:

$$\phi_{MBn}^e = \tan^{-1} \left( f_{MBny}^e / f_{MBnx}^e \right) \tag{15}$$

The rotor/TDB contact force at the measurement system location was not used directly in performing the static calibration. However, an estimate of the contact force,  $\mathbf{f}_c^e$ , may be inferred for an estimated AMB 2 force,  $\mathbf{f}_{MB}^e$ , according to

$$\mathbf{f}_c^e(0) = \left( \frac{l_1 - l_2}{l_1} \right) \mathbf{f}_{MB}^e(0) \tag{16}$$

### 5. Dynamic results

The results obtained from the static tests demonstrate the relationship between static input AMB 2 forces and estimated AMB 2 forces due to rotor/TDB contact. Dynamic force cases can also be investigated over different frequencies by employing the static calibration matrix with a dynamic scalar factor,  $\alpha(\hat{\mathbf{f}}_{MB}, \omega)$ , as indicated in Fig. 3. In effect, the dynamic calibration matrix, for a given AMB force level, is given by

$$\mathbf{C}_{MB}^e(\omega) = \mathbf{C}_{MB}^e(0) / \alpha(\hat{\mathbf{f}}_{MB}, \omega) \tag{17}$$

The procedure is to apply dynamic forces through AMB 2 and deduce  $\alpha(\hat{\mathbf{f}}_{MB}, \omega)$  in association with strain measurement system outputs. This will enable the estimation of AMB forces due to dynamic contact. Fig. 4(b) shows the general case of the rotor in contact with the bronze bushing at the strain measurement location. The rotor applies normal and tangential (friction) contact force components at the angle of contact  $\theta$  expressed as

$$\theta = \omega t + \phi \tag{18}$$

where  $\phi$  is a phase angle.

#### 5.1. Pseudo-dynamic force estimation

The static calibration matrix  $\mathbf{C}_{MB}^e(0)$  can be employed to define the estimated pseudo-dynamic AMB force due to dynamic contact

$$\mathbf{f}_{MB}^{ep}(t) = \mathbf{C}_{MB}^e(0) \hat{\mathbf{v}}(t) \tag{19}$$

The  $x$  and  $y$  components of the estimated pseudo-dynamic AMB force are expressed as

$$\mathbf{f}_{MB}^{ep}(t) = \begin{bmatrix} f_{MBx}^{ep}(t) \\ f_{MBy}^{ep}(t) \end{bmatrix} = \begin{bmatrix} F_{MBx}^{ep}(\omega) \cos(\omega t + \phi_{MBx}^{ep}(\omega)) \\ F_{MBy}^{ep}(\omega) \sin(\omega t + \phi_{MBy}^{ep}(\omega)) \end{bmatrix} \tag{20}$$

The force applied through AMB 2 is considered to be circular and with zero phase:

$$\hat{\mathbf{f}}_{MB}(t) = \begin{bmatrix} \hat{f}_{MBx}(t) \\ \hat{f}_{MBy}(t) \end{bmatrix} = \begin{bmatrix} \hat{F}_{MB} \cos \omega t \\ \hat{F}_{MB} \sin \omega t \end{bmatrix} = \hat{F}_{MB} \mathbf{e} \tag{21}$$

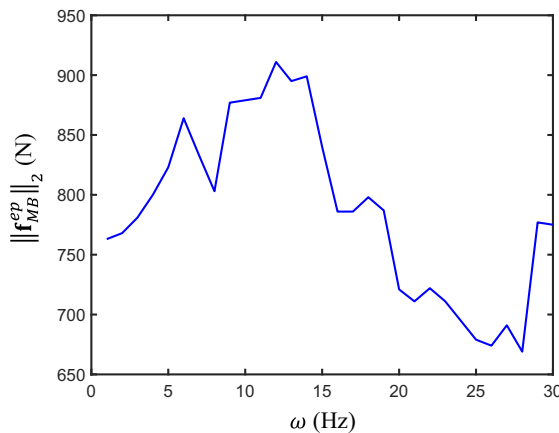
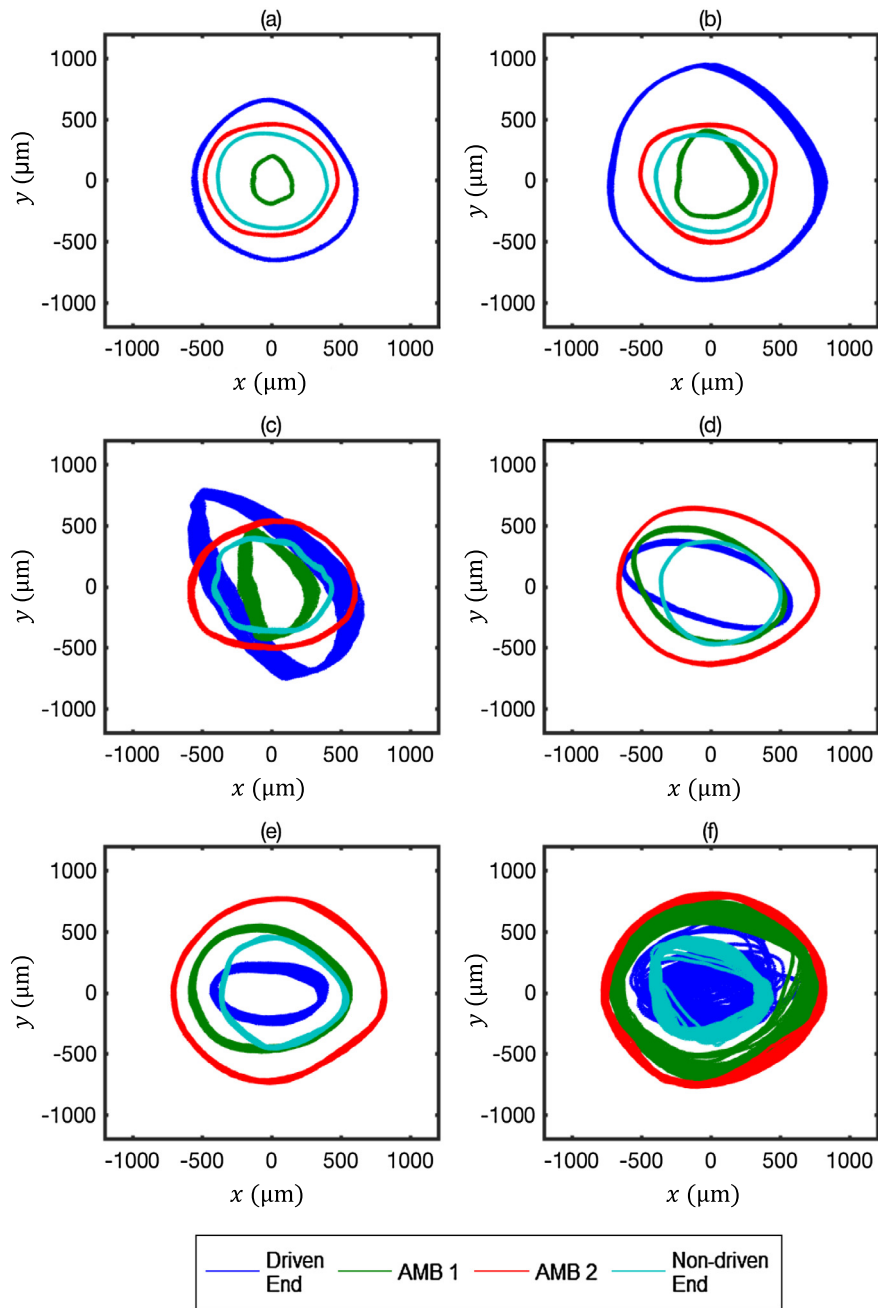


Fig. 11. Estimated pseudo-dynamic AMB 2 forces over a frequency range of 1–30 Hz for an applied AMB 2 force input of 700 N.



**Fig. 12.** Rotor orbits at the four sensor plane locations for an applied AMB 2 circular input force of 700 N at (a) 5 Hz (b) 10 Hz (c) 15 Hz (d) 20 Hz (e) 25 Hz (f) 30 Hz.

where  $\mathbf{e} = (\cos \omega t, \sin \omega t)^T$ . These forces may be applied under zero rotation conditions, the applied frequency  $\omega$  considered to be equivalent to a rotational frequency that would give rise to unbalance excitation. The dynamic scalar factor may then be obtained by comparing  $\mathbf{f}_{MB}^{ep}(t)$  and  $\hat{\mathbf{f}}_{MB}(t)$ :

$$\alpha(\hat{F}_{MB}\mathbf{e}, \omega) = \|\mathbf{f}_{MB}^{ep}(t)\|_2 / \|\hat{\mathbf{f}}_{MB}(t)\|_2 = \|\mathbf{f}_{MB}^{ep}(t)\|_2 / \hat{F}_{MB} \tag{22}$$

where  $\|\cdot\|_2$  denotes the Euclidean 2-norm. This scalar factor is frequency dependent, and may also vary for different input force amplitudes,  $\hat{F}_{MB}$ . It is then permissible to write the estimated dynamic AMB force as

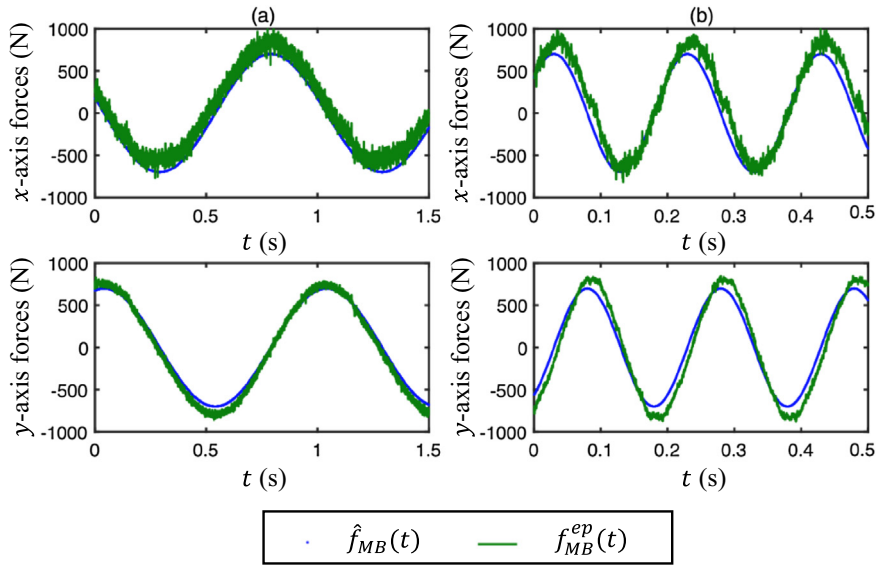


Fig. 13. Estimated pseudo-dynamic and input AMB 2 forces for an applied input amplitude of 700 N at (a) 1 Hz (b) 5 Hz.

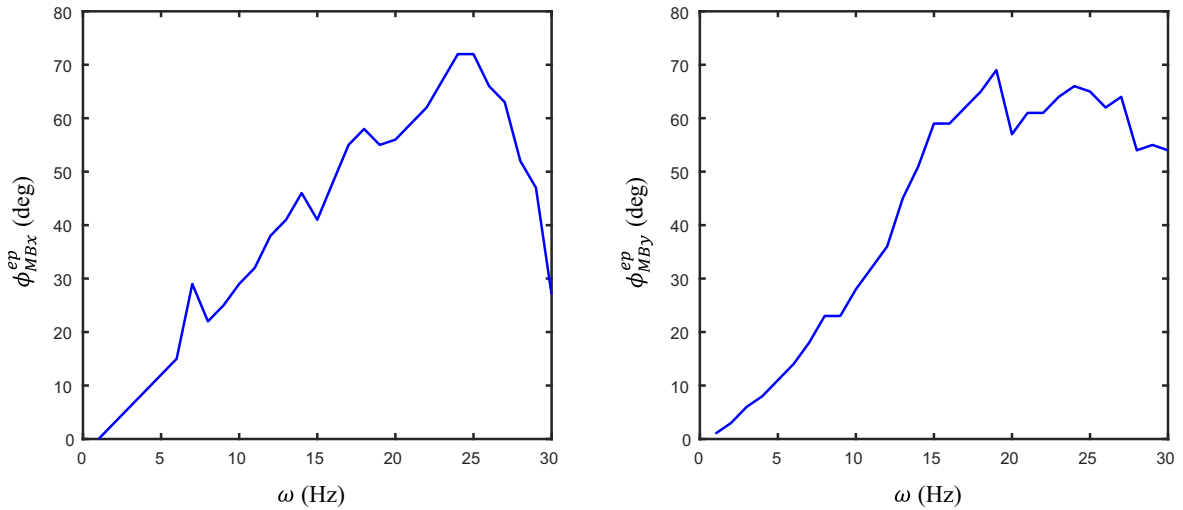


Fig. 14. Phase difference between input and estimated pseudo-dynamic AMB 2 forces in x and y components for an applied AMB 2 force input of 700 N.

$$\mathbf{f}_{MB}^e(t) = \mathbf{f}_{MB}^{ep}(t) / \alpha(\hat{\mathbf{F}}_{MB} \mathbf{e}, \omega) \tag{23}$$

Fig. 9 shows the x and y components of the estimated pseudo-dynamic AMB 2 forces, where an AMB force input amplitude of 700 N was applied at whirl frequencies of 1 Hz and 5 Hz. This demonstrates dynamic measurement system outputs. Dynamic input forces were applied through AMB 2 while full PID control action at both AMBs was functional. Considering a range of forces, the relationships between input and estimated pseudo-dynamic AMB forces for whirl frequencies of 1 and 10 Hz were obtained as shown in Fig. 10. An AMB 2 input force amplitude range of 100–1200 N was applied. A linear force relationship in each case is evidenced. A first order polynomial fit to each plot yields the dynamic scalar factor  $\alpha(\hat{\mathbf{f}}_{MB}, \omega)$  for that specific frequency. At 1 Hz,  $\alpha(\hat{\mathbf{f}}_{MB}, \omega)$  was found to be 1.33, while at 10 Hz,  $\alpha(\hat{\mathbf{f}}_{MB}, \omega)$  was found to be 1.27. This scalar factor may thus vary at different frequencies and at different force levels.

To examine the frequency response, further tests were performed with a whirl frequency range of 1–30 Hz, covering different rotor critical speed frequencies, with a constant input AMB force amplitude. The relationship between input AMB 2

forces and estimated pseudo-dynamic AMB 2 forces was considered. Fig. 11 shows the dynamic behaviour of the system at an AMB 2 applied input force amplitude of 700 N. Frequency dependence is noticed in Fig. 11. The estimated pseudo-dynamic AMB force amplitude at 1 Hz is evaluated to be 763 N giving  $\alpha(\hat{\mathbf{f}}_{MB}, \omega) = 1.09$ , while at 12 Hz an estimated pseudo-dynamic AMB force amplitude of 911 N indicates that  $\alpha(\hat{\mathbf{f}}_{MB}, \omega) = 1.30$ . The peaks at 12–13, 18 and 29 Hz in Fig. 11 are variants of the contact-free natural frequencies of the levitated rotor stated in Section 2. These represent rotor modes with rigid body dominance, in addition to a mode having significant rotor flexure. A peak at approximately 7 Hz is also evident, which was attributed to base motion of the test rig support structure, which is mounted on isolators to ground. Thus rotor/TDB contact may induce base motion.

Fig. 12 shows the rotor orbits at the four displacement sensor locations along the rotor for a 700 N AMB 2 input force amplitude. The rotor is in contact with the TDB at the strain measurement system location (non-driven end) at each frequency considered. No rotor/TDB contact occurs at AMB 1 due to the PID integral control action, nor does rotor/TDB contact occur at the driven end TDB due to the larger rotor/TDB radial clearance. The rotor makes contact at the TDB of AMB 2, where the input force is applied, at frequencies of 25 and 30 Hz. This is due to the combination of a 700 N force amplitude and amplification of whirl orbits associated with the rotor flexural mode. Hence multiple contact locations can occur along the rotor.

The test results were generally repeatable over the range of excitation frequencies considered and in the presence of the modal damping provided by the AMBs. It is noted that reduced modal damping may give rise to stronger bounce-like rotor motions and hence more fluctuations in contact induced responses.

## 5.2. Phase estimation

In order to fully understand rotor/AMB/TDB dynamics and enable potential contact control, the phases associated with the estimated pseudo-dynamic AMB force outputs need to be determined. Both input AMB forces and strain measurement system outputs have been applied and measured in their  $x$  and  $y$  components. This can enable the evaluation of phase differences. Fig. 13 shows input and estimated pseudo-dynamic AMB force components for 700 N AMB 2 applied forcing at whirl frequencies of 1 Hz and 5 Hz. Phase difference in the time domain between applied input forces and estimated pseudo-dynamic AMB forces in the  $x$  and  $y$  directions can be identified. This yields experimental phase data for each frequency. At 1 Hz, a phase difference of 1 deg exists, while at 5 Hz, a phase difference of 11 deg is evaluated. In this case, the dynamic scalar factor  $\alpha(\hat{\mathbf{f}}_{MB}, \omega)$  is evaluated to be 1.09 at 1 Hz, and 1.17 at 5 Hz. The dynamic scalar factor and phase obtained at 1 Hz represent nearly static conditions. This is less so at 5 Hz, with a bigger phase difference and an increased dynamic scalar factor value. The phase differences may be attributed to the rotor/AMB system dynamics together with contact friction between the rotor and the TBD, which is absent during the static tests. This includes the influence of system critical frequencies and rotor mode shapes.

Fig. 14 shows the phase difference between the estimated pseudo-dynamic AMB forces and applied forces, in both the  $x$  and  $y$  components, for a whirl frequency range of 1–30 Hz and an applied AMB 2 input force amplitude of 700 N. There is a small difference between the phase values in the  $x$  and  $y$  components at some frequencies. It is useful to arrive at an overall resultant phase difference value at each frequency for the input force level considered. The different  $x$  and  $y$  components of

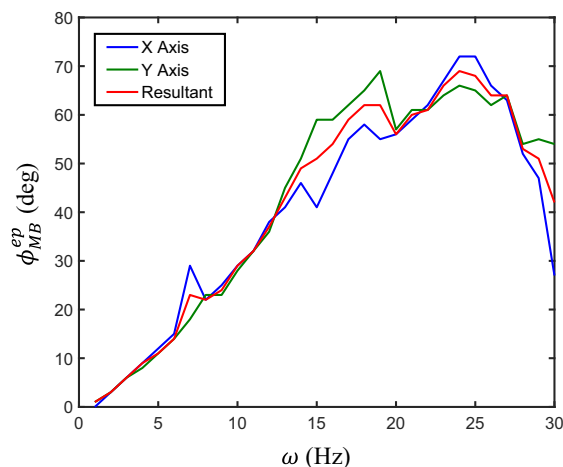
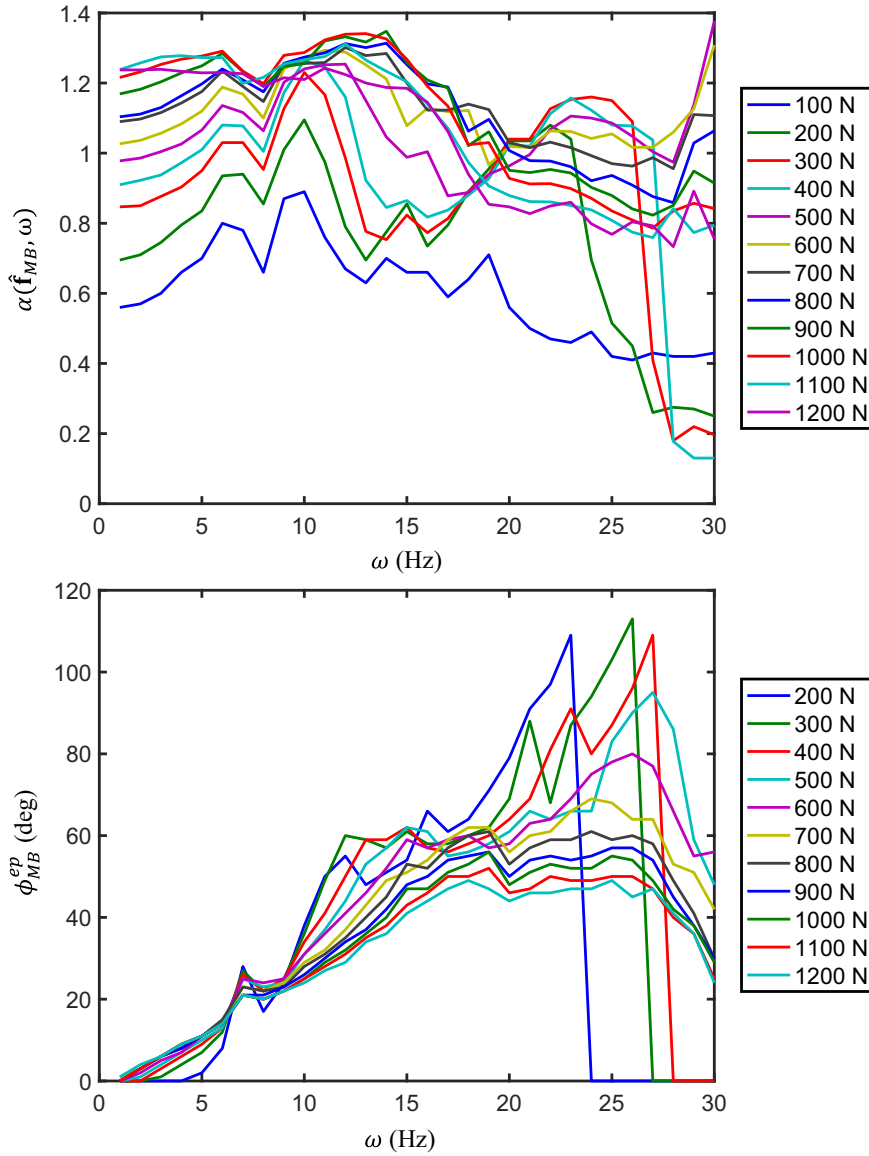


Fig. 15. Phase differences between input and estimated pseudo-dynamic AMB 2 forces for an applied AMB 2 force input of 700 N.



**Fig. 16.** Dynamic scalar factors and phase differences between input AMB 2 forces and estimated pseudo-dynamic AMB 2 forces for a frequency range of 1–30 Hz and input force amplitudes of 100–1200 N.

the estimated pseudo-dynamic AMB force of Eq. (20) can be considered. The resultant overall phase difference,  $\phi_{MB}^{ep}$ , can be calculated by considering the rotor forward whirl motion:

$$\phi_{MB}^{ep}(\omega) = \tan^{-1} \left( \frac{F_{MBx}^{ep}(\omega) \sin \phi_{MBx}^{ep}(\omega) + F_{MBy}^{ep}(\omega) \sin \phi_{MBy}^{ep}(\omega)}{F_{MBx}^{ep}(\omega) \cos \phi_{MBx}^{ep}(\omega) + F_{MBy}^{ep}(\omega) \cos \phi_{MBy}^{ep}(\omega)} \right) \quad (24)$$

Using Eq. (24), the results of Fig. 14 are combined with the resultant phase and shown in Fig. 15. The frequency dependent nature of the phase difference is evident. Since phase data are demonstrated using dynamic outputs, devising AMB control forces with the appropriate phases is potentially achievable for rotor/TDB contact control.

### 5.3. System frequency response

The initial tests performed were extended to cover a variety of force levels and frequencies, yielding more force and phase data in relation to AMB input forces. This provides experimental data for a range of contact conditions caused by different input disturbances. Dynamic AMB 2 input forces were applied with an amplitude range of 100–1200 N with 100 N incre-

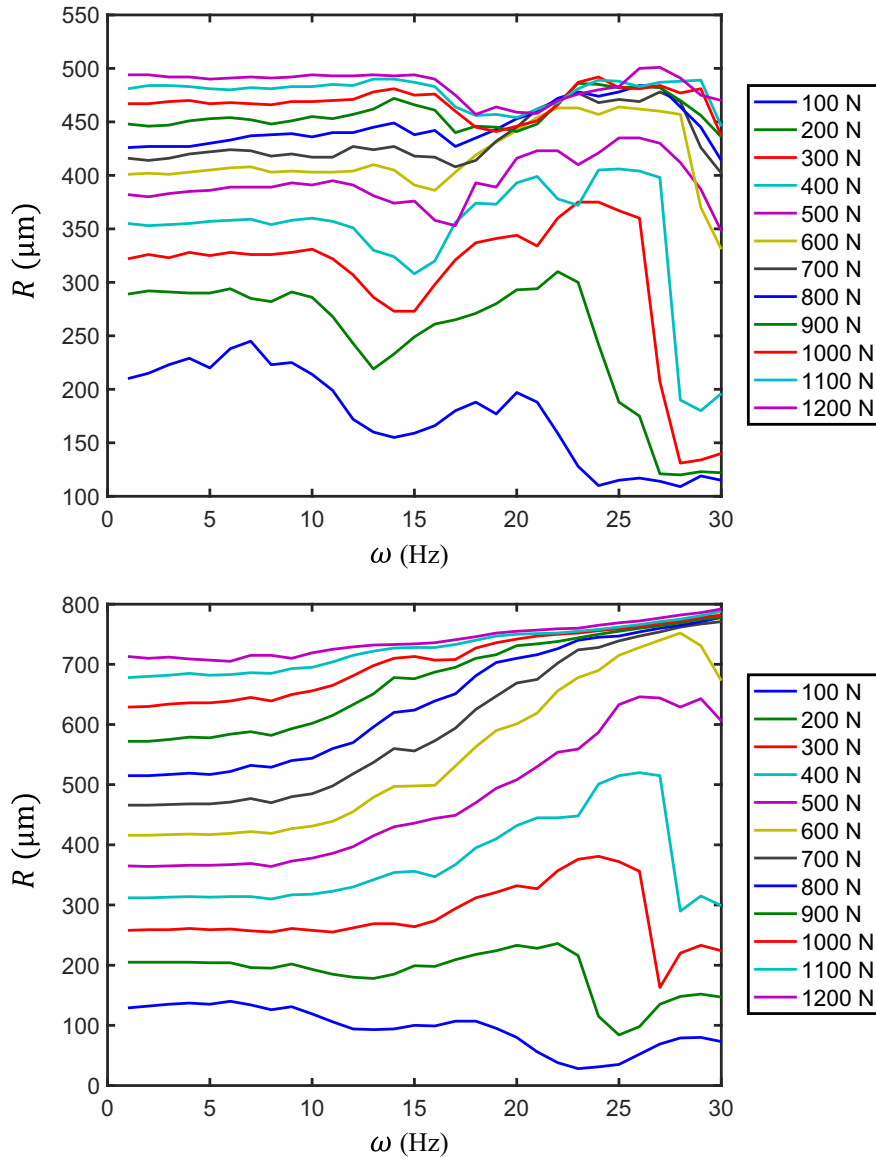


**Fig. 17.** Rotor displacement amplitudes at the non-driven end (top) and at AMB 2 (bottom) for a frequency range of 1–30 Hz and AMB 2 input force amplitudes of 100–1200 N.

ments. An input whirl frequency range of 1–30 Hz with 1 Hz increments was applied for each force amplitude. Thus, 360 individual experimental tests were performed to arrive at the full set of data.

Grease lubrication was used between the rotor and the TDB at the strain measurement system location, giving a relatively low coefficient of friction and reducing damage to the system due to the contact motion. Fig. 16 shows the dynamic scalar factor  $\alpha(\hat{\mathbf{f}}_{MB}, \omega)$  and the corresponding phase difference  $\phi_{MB}^{ep}$  for each input force amplitude and frequency.

Displacement sensor data were recorded to show the corresponding rotor displacement amplitudes. Figs. 17 and 18 show the radial displacement amplitudes at different locations along the 2 m flexible rotor. The radial displacement amplitude for each input force level and frequency was calculated by

$$R = \sqrt{x^2 + y^2} \quad (25)$$

It is noted from Fig. 16 that the dynamic scalar factor  $\alpha(\hat{\mathbf{f}}_{MB}, \omega)$  varies at different force levels in addition to being frequency dependent. The same applies in relation to the phase difference  $\phi_{MB}^{ep}$ . The rotor displacement amplitudes in Figs. 17 and 18 show that no rotor/TDB contact occurs at AMB 1 or at the driven end over the force and whirl frequency range con-

sidered. However, contact does occur at the AMB 2 TDB at high input force amplitudes and frequencies, where the rotor/TDB clearance is 0.75 mm. This demonstrates that multiple rotor/TDB contact locations may occur along the rotor, since contact also happens at the non-driven end. Full rotor/TDB contact occurs at most force levels and frequencies at the non-driven end, where the strain measurement system is, as the results demonstrate. This is due to the small rotor/TDB clearance. However, for input forces of 400 N and below, full rubbing contact does not occur at all force levels and frequencies. Although the rotor/TDB radial clearance at the strain measurement system was 0.35 mm, displacement amplitudes attain approximately 0.5 mm at the non-driven end (Fig. 17). This is because the displacement sensors are not at the same position as the strain measurement system along the rotor (see Fig. 2), and both the rotor and the strain measurement system have degrees of flexibility.

The force, phase and displacement data presented evidence the rotor passing through different modes and critical frequencies, while it is levitated with the PID controlled AMBs, identifying the rotor system dynamics in contact cases.

#### 5.4. Control force estimation

For a pseudo-dynamic AMB force  $\mathbf{f}_{MB}^{ep}$  arising due to contact, the estimated AMB force  $\mathbf{f}_{MB}^c$  could represent an AMB control force, which if appropriately phased, has the potential to recover the rotor from contact. In order to evaluate  $\mathbf{f}_{MB}^c$ , as indicated

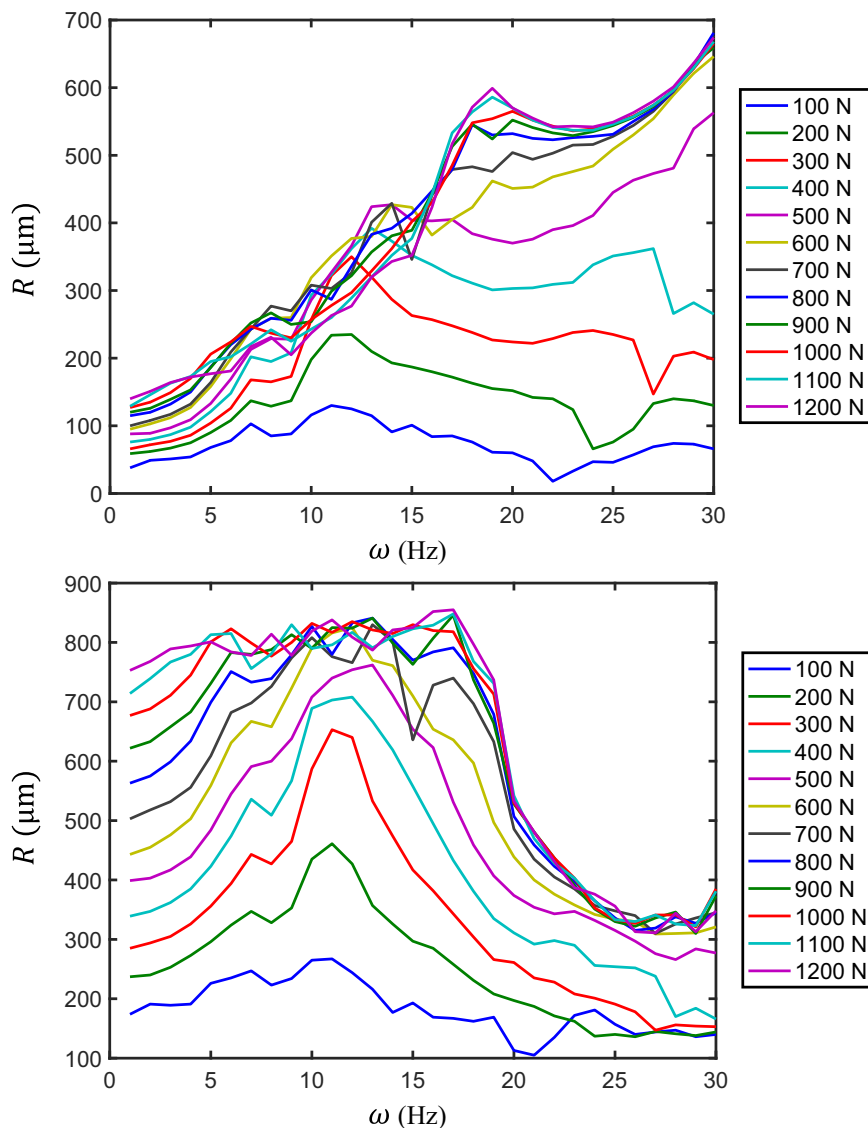


**Fig. 18.** Rotor displacement amplitudes at AMB 1 (top) and at the driven end (bottom) for a frequency range of 1–30 Hz and AMB 2 input force amplitudes of 100–1200 N.

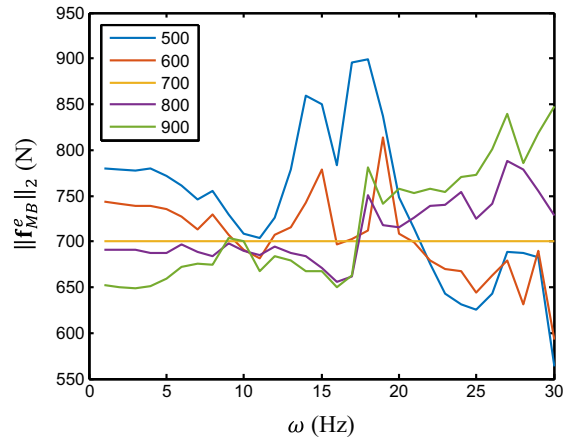


**Fig. 19.** Estimated AMB 2 forces corresponding to an input force of 700 N evaluated with different dynamic scalar factors corresponding to an input force range of 500–900 N.

in Fig. 3, the appropriate value of  $\alpha(\hat{\mathbf{f}}_{MB}, \omega)$  needs to be used. This can be achieved by considering different possible values of  $\alpha(\hat{\mathbf{f}}_{MB}, \omega)$  (Fig. 16) for a given force  $\mathbf{f}_{MB}^{ep}$ .

Forces  $\mathbf{f}_{MB}^{ep}$  corresponding to contact caused by an input AMB force of 700 N over a frequency range of 1–30 Hz (see Fig. 11) were considered to arrive at the forces  $\mathbf{f}_{MB}^e$ . Fig. 19 shows five different force amplitudes  $\|\mathbf{f}_{MB}^{ep}\|_2$  at each frequency, which were evaluated using  $\|\mathbf{f}_{MB}^{ep}\|_2$  and five different possible values of  $\alpha(\hat{\mathbf{F}}_{MB}\mathbf{e}, \omega)$ . The values of  $\alpha(\hat{\mathbf{F}}_{MB}\mathbf{e}, \omega)$  used correspond to a range of input AMB forces of amplitudes 500–900 N. The estimated AMB forces  $\mathbf{f}_{MB}^e$  were evaluated according to Eq. (23) with  $\alpha(500\mathbf{e}, \omega)$ ,  $\alpha(600\mathbf{e}, \omega)$ ,  $\alpha(700\mathbf{e}, \omega)$ ,  $\alpha(800\mathbf{e}, \omega)$  and  $\alpha(900\mathbf{e}, \omega)$  signifying the dependence on the input force amplitude. Fig. 19 shows that  $\alpha(700\mathbf{e}, \omega)$ , corresponding to an input AMB force of amplitude 700 N, gives rise to a constant value of  $\|\mathbf{f}_{MB}^{ep}\|_2$  of 700 N over the frequency range, while other values of  $\alpha$  cause the estimated AMB force levels to deviate. It can be seen that  $\|\mathbf{f}_{MB}^{ep}\|_2$  is equal or close to a certain input AMB force level, over the whole frequency range, when the appropriate  $\alpha(\hat{\mathbf{F}}_{MB}\mathbf{e}, \omega)$  is used. Thus, the correct value of  $\mathbf{f}_{MB}^e$  can be determined from a force  $\mathbf{f}_{MB}^{ep}$  by applying this scalar factor.

It is noted that certain peaks are evident in the plots of Fig. 19, excepting the “exact” case of 700 N. In Section 2, contact-free levitated modes of the rotor/AMB/base frame system on isolators are indicated at 7 Hz, 12 Hz, 17 Hz and 27 Hz. These modes are modified under contact as evident when the dynamic scalar factor,  $\alpha(\hat{\mathbf{f}}_{MB}, \omega)$ , corresponds with an input force that is different from the actual value. There are slight modifications to natural frequencies under contact, e.g. 13–15 Hz and 17–19 Hz, but they can be attributed to the rotor dynamics rather than the higher frequency strain measurement system. It is acknowledged that testing of higher speed rotors may necessitate modifications to the strain measurement system to ensure that no crossover of its dynamics occurs. Therefore, the dynamic results presented in this paper, covering a range of force levels at various operating frequencies, represent appropriate system identification for the particular rotor/TDB contact cases considered.

## 6. Conclusions

This paper has demonstrated a new method to assess experimentally rotor/TDB contact. A strain measurement system is specified and it was employed on an AMB system with a long flexible rotor. Strain measurements of the TDB support structure are related to rotor/TDB contact force components and then to applied AMB forces through a static calibration procedure. Dynamic rotor/TDB contact cases are investigated using applied AMB unbalance forces. The strain measurement system is shown to estimate pseudo-dynamic AMB forces and phases due to contact, based on the static calibration. The frequency dependent behaviour of the rotor/AMB/TDB system was investigated in contact conditions over a frequency range covering three rotor critical frequencies. Force, phase, and displacement data are presented and discussed. The estimation of dynamic AMB control forces upon rotor/TDB contact is established. Although rotor displacement data are typically used in assessing rotor/TDB contact in AMB systems, experimental quantification of forces in contact conditions can provide a number of benefits, including:

- Force data can confirm rotor/TDB contact occurrence and contact modes, while rotor displacement orbits may not give a clear indication of contact in some cases

- Changes in rotor/TDB contact force levels, and thus the stresses/strains affecting the system, are difficult to determine using rotor orbits, except by audible contact becoming evident. Experimental force data can provide such information
- Evaluation of force levels can provide improved system monitoring and diagnosis, particularly in relation to touchdown bearings
- Force data can be potentially directly employed in control strategies employing AMB forces, while further analysis is needed if displacement data are employed.

The results demonstrated in this paper represent system identification, and can be utilised in the design and application of new control methods employing synchronous unbalance compensation AMB forces to achieve rotor/TDB contact recovery. This would optimise finite duration contact control in fully operational AMB systems that experience intermittent faults or external inputs or disturbances, particularly those that lead to persistent contact.

## Acknowledgement

The authors acknowledge the support of the EPSRC (UK) through the funding this research under grant EP/D031389/1.

## References

- [1] J. Schmied, J.C. Pradetto, Behavior of a one ton rotor being dropped into auxiliary bearings, Third International Symposium on Magnetic Bearings, Alexandria, VA, 1992, pp. 145–156.
- [2] R.G. Kirk, T. Ishii, Transient rotor drop analysis of rotors following magnetic bearing power outage, MAG'93 – Magnetic Bearings, Magnetic Drives and Dry Gas Seals Conference and Exhibition, Alexandria, VA, 1993, pp. 53–61.
- [3] E.E. Swanson, R.G. Kirk, J. Wang, AMB rotor drop initial transient on ball and solid bearings, Proceedings of MAG'95, Alexandria, VA, 1995, pp. 207–216.
- [4] L. Hawkins, A. Filatov, S. Imani, D. Prosser, Test results and analytical predictions for rotor drop testing of an active magnetic bearing expander/generator, ASME J. Eng. Gas Turbines Power 129 (2007) 522–529.
- [5] G. Sun, A.B. Palazzolo, A. Provenza, G. Montague, Detailed ball bearing model for magnetic suspension auxiliary service, J. Sound Vib. 269 (3–5) (2004) 933–963.
- [6] J. Anders, P. Leslie, L. Stacke, Rotor drop simulations and validation with focus on internal contact mechanisms of hybrid ball bearings, ASME Turbo Expo, Texas, 2013, Paper GT2013-95816.
- [7] W.C. Foiles, P.E. Allaire, Nonlinear transient modelling of active magnetic bearing rotors during rotor drop on auxiliary bearings, in: Proceedings of MAG'97, Alexandria, VA, 1997, pp. 154–163.
- [8] R.G. Kirk, Evaluation of AMB turbomachinery auxiliary bearings, ASME J. Vib. Acoust. 121 (1999) 156–161.
- [9] M.O.T. Cole, P.S. Keogh, Asynchronous periodic contact modes for rotor vibration within an annular clearance, Proc. IMechE, Part C 217 (2003) 1101–1115.
- [10] G. Jacquet-Richardet, M. Torkhani, P. Cartraud, F. Thouverez, T. Nouri Baranger, M. Herran, C. Gibert, S. Baguet, P. Almeida, L. Peletan, Rotor to stator contacts in turbomachines. Review and application, Mech. Syst. Sig. Process. 40 (2013) 401–420.
- [11] H.F. Black, Interaction of a whirling rotor with a vibrating stator across a clearance annulus, J. Mech. Eng. Sci. 10 (1) (1968) 1–12.
- [12] A.R. Bartha, Dry friction induced backward whirl: Theory and experiment, in: Proceedings of 5th IFToMM Conference on Rotor Dynamics, Darmstadt, 1998, 756–767.
- [13] A. Muszynska, Rotor-to-stationary part full annular contact modeling, in: Proceedings of 9th International Symposium on Transport Phenomena and Dynamics of Rotating Machinery, Honolulu, Hawaii, 2002.
- [14] P. Pennacchi, N. Bachtshmid, E. Tanzi, Light and short arc rubs in rotating machines: experimental tests and modelling, Mech. Syst. Sig. Process. 23 (2009) 2205–2227.
- [15] F. Wu, G.T. Flowers, An experimental study of the influence of disk flexibility and rubbing on rotordynamics, Proceedings of ASME Conference on Vibrations of Rotating Systems, 1993, pp. 19–26.
- [16] Y.B. Kim, S.T. Noah, Bifurcation analysis for a modified Jeffcott rotor with bearing clearances, Nonlinear Dyn. 1 (1990) 221–241.
- [17] X. Wang, S.T. Noah, Nonlinear dynamics of a magnetically supported rotor on safety auxiliary bearings, ASME J. Vib. Acoust. 120 (1998) 596–606.
- [18] J.G. Lee, A. Palazzolo, Catcher bearing life prediction using a rainfall counting approach, ASME J. Tribol. 134 (2012), 031101–031101 15.
- [19] S. Lahrii, I.F. Santos, H.I. Weber, H. Hartmann, On the nonlinear dynamics of two types of backup bearings: theoretical and experimental aspects, ASME J. Eng. Gas Turbines Power 134 (11) (2012), 112503–112503-13.
- [20] C. Jarroux, R. Dufour, J. Mahfoud, B. Defoy, T. Alban, A. Delgado, On the drop of a rotor-amb system onto touch-down bearing, in: Proceedings of the Vibrations in Rotating Machinery Conference (VIRM), Manchester, UK, 2016, pp. 671–681.
- [21] C. Jarroux, R. Dufour, J. Mahfoud, B. Defoy, T. Alban, A. Delgado, Non-linear models for rotor-amb system drop, Third International Conference on Structural Nonlinear Dynamics and Diagnosis (CSNDD), Marrakech, Morocco, 2016, Paper No. 05005.
- [22] P.S. Keogh, M.O.T. Cole, Rotor vibration with auxiliary bearing contact in magnetic bearing systems, Part 1: Synchronous dynamics, Proc. Inst. Mech. Eng., Part C: J. Mech. Eng. Sci. 217 (2003) 377–392.
- [23] M.O.T. Cole, P.S. Keogh, Rotor vibration with auxiliary bearing contact in magnetic bearing systems, Part 2: Robust synchronous control for rotor position recovery, Proc. Inst. Mech. Eng., Part C: J. Mech. Eng. Sci. 217 (2003) 393–409.
- [24] I.S. Cade, M.N. Sahinkaya, C.R. Burrows, P.S. Keogh, On the design of an active auxiliary bearing for rotor/magnetic bearing systems, Proceedings of ISMB 11, Nara, Japan, 2008.
- [25] P.S. Keogh, Contact dynamic phenomena in rotating machines: active/passive considerations, Mech. Syst. Sig. Process. 29 (2012) 19–33.
- [26] P. Li, M. Sahinkaya, P. Keogh, Active touchdown bearing control for recovery of contact-free rotor levitation in AMB systems, The 14th International Symposium on Magnetic Bearings – ISMB14, Linz, Austria, 2014, pp. 115–120.
- [27] H. Ulbrich, A. Chavez, R. Dhima, Minimization of contact forces in case of rotor rubbing using an actively controlled auxiliary bearing, Proceedings of the 10th International Symposium on Transport Phenomena and Dynamics of Rotating Machinery, Honolulu, Hawaii, 2004, pp. 1–10.
- [28] L. Ginzinger, H. Ulbrich, Control of a rubbing rotor using an active auxiliary bearing, J. Mech. Sci. Technol. 21 (6) (2007) 851–854.
- [29] A.G. Abulrub, M.N. Sahinkaya, C.R. Burrows, P.S. Keogh, Adaptive control of active magnetic bearings to prevent rotor-bearing contact, ASME International Mechanical Engineering Congress and Exposition, Dynamic Systems and Control, Parts A and B, Chicago, 2006, pp. 1523–1529.
- [30] M. Sahinkaya, A.G. Abulrub, C.R. Burrows, P.S. Keogh, A multiobjective adaptive controller for magnetic bearing systems, ASME, J. Eng. Gas Turbines Power 132 (12) (2010), pp. 122503–122503-7.
- [31] M. Fumagalli, P. Varadi, G. Schweitzer, Impact dynamics of high speed rotors in retainer bearings and measurement concepts, in: Proceedings of ISMB 4, ETH Zurich, 1994, pp. 239–244.
- [32] E.N. Cuesta, V.R. Rastelli, L.U. Medina, N.I. Montbrun, S.E. Diaz, Non-linear behaviors in the motion of a magnetically supported rotor on the catcher bearing during levitation loss: an experimental description, ASME Turbo Expo 4 (2002) 607–614, Amsterdam.
- [33] S. Lahrii, I.F. Santos, Experimental quantification of contact forces with impact, friction and uncertainty analysis, Tribol. Int. 66 (2013) 93–104.

- [34] C.A. Fonseca, I.F. Santos, H.I. Weber, Influence of unbalance levels on nonlinear dynamics of a rotor-backup rolling bearing system, *J. Sound Vib.* 394 (2017) 482–496.
- [35] M. Fumagalli, Modelling and measurement analysis of the contact interaction between a high speed rotor and its stator, Swiss Institute of Technology Zurich (1997) (Doctoral Dissertation).
- [36] D. Kwapisz, J. Stephant, D. Meizel, Instrumented Bearing for Force and Moment Measurements, *IEEE Sensors*, Lecce, Italy, 2008, pp. 1480–1483.